This article has been accepted for publication in IEEE Transactions on Power Electronics. This is the author's version which has not been fully edited and content may change prior to final publication. Citation information: DOI 10.1109/TPEL.2025.3591384

A Novel Flying Inductor-Based Universal Converter Topology

Naser Vosoughi Kurdkandi, *Member, IEEE,* Sze Sing Lee, *Senior Member, IEEE,* Oleksandr Husev, *Senior Member, IEEE,* Zhi Cao, *Member, IEEE,* Chunting Chris Mi, *Fellow, IEEE*

***Abstract*- A novel single-phase converter topology based on a flying inductor is proposed in this paper. The proposed converter has buck and boost functionalities and can adapt to a wide range of input voltage changes. The converter has a dynamic voltage gain and can provide a fixed AC voltage output with different DC input voltages. Common coupling is established between the input and output, which is very suitable in renewable energy systems (RES) where the isolation can be eliminated. The absence of electrolytic capacitors can contribute to the longevity of the converter. Non-unity power factor loads can be fed by the proposed converter. In addition, the single-stage power processing makes the proposed converter a suitable interface between AC and DC microgrids and can achieve extremely high efficiency. The operating modes and design of passive elements have been fully investigated in this paper. To show the advantages of the proposed converter, a comparison has been made with other converters. Finally, to validate the performance of the proposed converter topology, an experimental setup of 3 kW/7 kW was built and the experimental results verified the theoretic analysis and demonstrated the superior performance of the proposed topology.**

***Index Terms*-** Single-phase, single-stage, flying inductor, buck-boost capability.

I. INTRODUCTION

The advent of AC transformers in the early days of electricity enabled the development of cost-effective, high-voltage transmission systems spanning long distances [1]. This achievement, coupled with the absence of DC-DC converters, resulted in the prevalence of AC over DC, shaping today's infrastructure around AC systems [2]. However, recent advancements in power electronic converters have rendered transformers unnecessary in many applications, as they are now considered inefficient and costly [3]. The emergence of DC-DC power converters at various levels has made it feasible to establish DC grids [4]-[5]. Unlike AC grids, DC grids do not face challenges such as harmonic suppression, skin effect, reactive power compensation, frequency, and voltage stabilization. Additionally, DC power systems are more compatible with renewable energy sources, energy storage systems, LED lighting, and electric vehicles due to their inherent DC nature [6]. Furthermore, the use of DC grids is more efficient and cost-effective compared to multistage AC power systems involving DC-DC and DC-AC converters [7]. DC power systems offer technical advantages such as higher efficiency, the absence of reactive power, and the elimination of bulky line-frequency transformers. Therefore, DC grids present a promising solution to the modern renewable-rich power girds [8]. Despite these benefits, the dominant use of AC remains a challenge, primarily due to the lack of a viable business model for DC grid implementation. Investors are hesitant to explore the potential applications of DC grids, while power electronics manufacturers are not rushing to produce DC appliances. Additionally, there is a lack of clear vision and specific standards for DC grids. Determining the appropriate voltage level for DC grids is also a subject of debate. Studies have suggested that 326, 350, and 380 volts are suitable DC voltage levels [9], [10]. Where 326V is the output voltage of the passive rectifier, 380V is the output voltage of the active rectifier or power factor correction plus passive rectifier, and 350V is the voltage between the midpoint and either of the positive or negative lines in three-wire DC systems. However, significant work is needed to finalize the necessary standards for DC grids. Consequently, DC is unlikely to fully replace AC in the near term, and the transition from AC to DC will be gradual and a hybrid power system will emerge, incorporating both DC and AC grids. Such a hybrid system, illustrated in Fig. 1, would allow for dynamic access to the available grid [3].

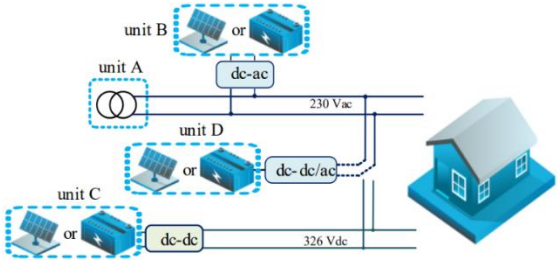

Fig. 1. Universal converter in a simplified hybrid power system [3].

The majority of current DC-AC inverters can serve as potential solutions for universal DC-DC/AC power conversion. In [11]-[12], universal DC-DC/AC power converters are presented, utilizing a buck-boost DC-DC converter with an unfolding circuit. The switches in the unfolding stage operate at a low grid frequency, minimizing switching losses. Additionally, these topologies use a low-value capacitor, contributing to higher power density. However, these solutions do not completely eliminate leakage current.

Among alternative solutions, there has been notable interest in impedance-source (IS)-based inverters. The Z-source inverter (ZSI), introduced in [13] as a single-stage solution, addresses the limitations of conventional grid-connected inverters by offering both buck and boost modes without encountering shoot-through (ST) states. Several other variations of IS networks have been suggested [14]-[15]. However, issues regarding the size of passive components and the stress of semiconductor devices have been noted [16], casting doubt on its practical application.

Some modifications of the current source inverter, as described in [17] and [18], are known as CH5 and CH7 topologies. These designs feature reduced leakage current and can operate at voltages below the peak of the grid voltage, but they have limited input voltage regulation capability and cannot control reactive power.

Switched-capacitor (SC) or flying capacitor (FC) structures are considered potential solutions with extended input voltage range regulation [19]-[29]. However, the structures proposed in [19]-[20] are unable to increase voltage, requiring a boost converter at

This article has been accepted for publication in IEEE Transactions on Power Electronics. This is the author's version which has not been fully edited and content may change prior to final publication. Citation information: DOI 10.1109/TPEL.2025.3591384

voltages below the peak of the grid voltage. Additionally, SC-based common ground structures suffer from inrush charge current issues, which reduce capacitor lifespan and necessitate larger switches and diodes. Reference [30] introduces a converter with Buck-boost capability, albeit with more energy storage elements.

Concurrently, there is a growing research focus on the reliability of power electronics [31]. One of the primary challenges lies in the reliability of converter components. Industrial experience indicates that converters are often sources of failure in various applications, such as wind and PV systems, primarily due to electrolytic capacitor failures. Consequently, there is a trend to mitigate this issue by substituting electronic capacitors for electrolytic ones and/or utilizing topologies that do not rely on large capacitance values. References [32]-[35] introduce some topologies based on the Flying Inductor (FI) concept, featuring buck-boost capability and eliminating the need for electrolytic capacitors.

In this paper, a novel converter topology based on a flying-inductor with buck-boost capability is presented. The buck-boost capability allows the converter to adapt a wide range of DC input voltages and perform the process of transferring power from input to output with single-stage power conversion. Common coupling between the input and the output, non-unity power factor load support, and bidirectionality are other features of the proposed converter topology, hence, making this converter as a possible solution for universal application.

The unique advantages of the proposed converter can be summarized as follows:

1. Buck-boot capability and dynamic voltage gain that can convert any DC voltage to a fixed AC or DC output.
2. Bidirectional capability that make it suitable for the battery-based energy storage system.
3. Common coupling between input and output that eliminates leakage current in the system.
4. Extremely high efficiency, reaching 99.2% in DC-DC mode and 97.7% in DC-AC mode.
5. Single-stage power conversion.
6. Heavy non-unity power factor load support.

The paper is organized as follows: In Sections II and III, the proposed converter topology and its operating modes are explained. In Section IV, design guidelines, current stress, and voltage stress of switches are discussed. In Section V, the proposed converter is compared with other converters. Finally, in Section VI, the performance of the proposed converter is validated by experimental results.

II. Proposed FI-Based Converter

The proposed circuit topology is shown in Fig. 3(a). This converter is proposed to generate AC and DC voltages at its output terminal without redundancy, which is very efficient for AC and DC microgrids. The proposed converter topology is based on flying inductor technology and does not have any electrolytic capacitors in the intermediate connections, which can help the converter's longevity. The proposed converter has buck-boost capability in a single-stage power conversion. Hence, the proposed converter can achieve a high efficiency and transfer power to the load or power grid in a wide range of input voltage without an additional boost converter. The proposed converter consists of eight MOSFET switches, an inductor, and a capacitor. The function of inductor L is to receive energy from the input DC voltage source and transfer it to the output side of the converter. The output capacitor C_f acts as a filter. Inductor L has a bidirectional current and the polarity of the current is different in the positive and negative half cycles. In this topology, the output filter consists of only one capacitor C_f and there is no inductor in the output of the converter. Therefore, the loss of the output filter is at its lowest value. Switches S_3 to S_8 act as four-quadrant switches and block voltage and current in two directions.

The solid-state circuit breaker (SSCB) switch is also a fast switch that can disconnect the converter from the AC and DC network side when necessary and during a fault. Since the proposed converter has bi-directional power capability, it is a very suitable interface for the Battery Energy Storage System (BESS) and can be placed between the power grid and the battery pack system on a domestic scale. The battery storage system can be charged from the power grid during low grid load times and return its energy to the grid at the peak of consumption. The direct connection between the positive terminal of the input source and the neutral terminal of the output power grid keeps the common mode voltage constant and eliminates the leakage current in the grid-connected photovoltaic system. Finally, the ability to reverse current in the proposed converter makes it possible to feed non-unity power factor loads with this converter or to control reactive power in grid-connected mode.

III. Operation Modes of the Proposed FI-Based Universal Converter

In this section, the operating modes of the proposed converter are explained. For the proposed topology, symmetric and asymmetric conditions can be considered. In symmetric conditions, the current of inductor L is equal in the positive and negative half cycle, while in asymmetric conditions, the inductor current in the positive and negative half cycle is not equal and has different values. In symmetric conditions, the proposed converter works in buck-boost mode in both positive and negative half cycles. While in asymmetric operation, the proposed converter works in buck-boost mode in the positive half-cycle and in buck mode and then boost mode in the negative half-cycle. When the input voltage is higher than the instantaneous value of the output voltage, the converter operates in buck mode in the negative half cycle, and when the input voltage is lower than the instantaneous value of the output voltage, the converter operates in boost mode. If the input voltage is higher than the peak value of the output voltage, the proposed converter acts as a buck converter in the entire negative half-cycle interval.

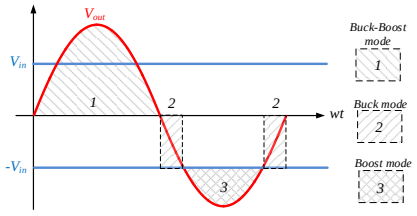

Fig. 2. Buck, boost, and buck-boost operation zones of the proposed converter.

Fig. 2 shows the operational principle of the proposed converter for asymmetric conditions. It can be seen from Fig. 2 that the proposed

converter topology works in the buck-boost mode for the first half-cycle, regardless of the input voltage, while the negative half-cycle performance depends on the input voltage. As shown in Fig. 2, the converter works in buck-boost mode in Area 1, in buck mode in Area 2, and in boost mode in Area 3.

A. Symmetric conditions, positive half cycle, and active mode

The equivalent circuit of the proposed converter in active mode and the positive half cycle is shown in Fig. 3(b). In this figure, switches S_2, S_3, and S_4 are on and cause inductor L to be charged by the input source. Switch S_8 is on, but no current passes through this switch. In this operating mode, the current of the load or grid closes its path from the output capacitor C_f.

B. Symmetric conditions, positive half cycle, and freewheeling mode

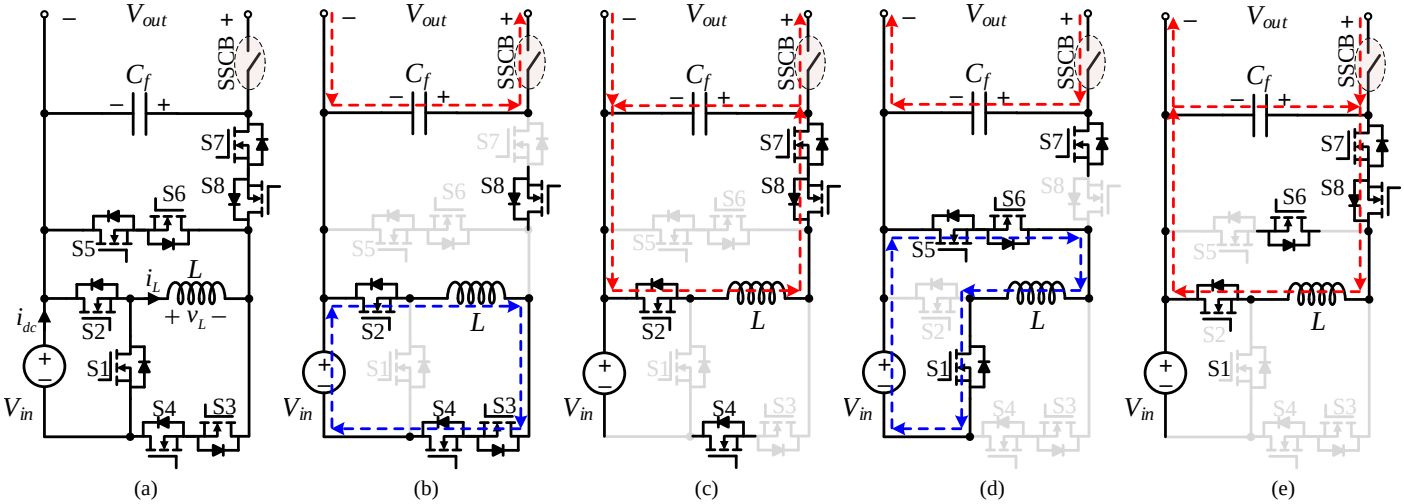

Fig. 3. (a) The proposed flying-inductor-based converter, operation modes of the proposed converter in symmetric conditions: (b) active mode in the positive half cycle, (c) freewheeling mode in the positive half cycle, (d) active mode in the negative half cycle, (e) freewheeling mode in the negative half cycle.

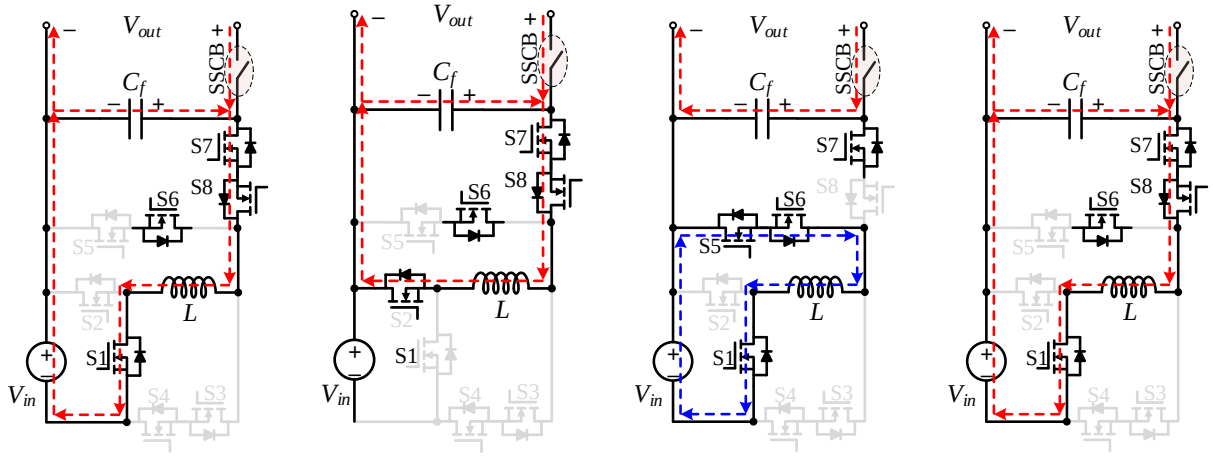

Fig. 4. Operation modes of the proposed converter in asymmetric conditions and negative half cycle: (a) active mode in buck state, (b) freewheeling mode in buck state, (c) active mode in boost state, (d) freewheeling mode in boost state.

The equivalent circuit of the proposed converter in freewheeling mode and the positive half cycle is shown in Fig. 3(c). In this figure, switches S_2, S_7, and S_8 are on and transfer the stored energy in inductor L to the output load and filter C_f. Switch S_4 is on, but its current is zero. In the positive half cycle and symmetric conditions, switches S_2, S_4, and S_8 are fully on, and switches S_3 and S_7 operate at the switching frequency.

C. Symmetric conditions, negative half cycle, and active mode

The equivalent circuit of the proposed converter in active mode and negative half cycle is shown in Fig. 3(d). In this operating mode, the current direction of inductor L is the opposite of the operating modes in the positive half cycle. Switches S_1, S_5, and S_6 are on and cause inductor L to be charged from the input source. Switch S_7 is also on in this operating mode, but its current is zero. In this working mode, the current of the load or grid closes its path from the output capacitor C_f.

D. Symmetric conditions, negative half cycle, and freewheeling mode

The equivalent circuit of the proposed converter in freewheeling mode and the positive half cycle is shown in Fig. 3(e). Switches S_2, S_7, and S_8 are on and release the stored energy in inductor L towards the output. Switch S_6 is also on in this working mode, but there is no current. In this mode, capacitor C_f is charged by inductor L. In the negative half cycle and symmetric conditions, switches S_6 and S_7 are fully on, and switches S_1, S_5, and S_8 operate at the switching frequency. As a general point, it can be stated that inductor L acts as an energy storage component in symmetric conditions. In other words, it stores energy in a portion of one switching cycle and

This article has been accepted for publication in IEEE Transactions on Power Electronics. This is the author's version which has not been fully edited and content may change prior to final publication. Citation information: DOI 10.1109/TPEL.2025.3591384

transfers its energy to the output in another portion of the switching cycle.

E. Asymmetric conditions, negative half cycle, and buck mode

In asymmetric conditions, the operating modes of the proposed converter in the positive half cycle are the same as in symmetric conditions and only the working modes in the negative half cycle are different. In the negative half cycle, when the instantaneous value of $|V_{out}|$ is lower than the input voltage, the converter operates in buck mode. In buck mode, inductor L acts as a filter. Fig. 4(a) shows the equivalent circuit of the proposed converter in active

Table I.
Duty cycle of switches in positive and negative half cycles

		S_1	S_2	S_3	S_4	S_5	S_6	S_7	S_8
Positive half cycle		0	1	$d_{Buck\text{-}Boost}(t)$	1	0	0	$1\text{-}d_{Buck\text{-}Boost}(t)$	1
Negative half cycle	$\|v_{out}\|<V_{in}$	$d_{Buck}(t)$	$1\text{-}d_{Buck}(t)$	0	0	0	1	1	1
	$\|v_{out}\|>V_{in}$	1	0	0	0	$d_{Boost}(t)$	1	1	$1\text{-}d_{Boost}(t)$

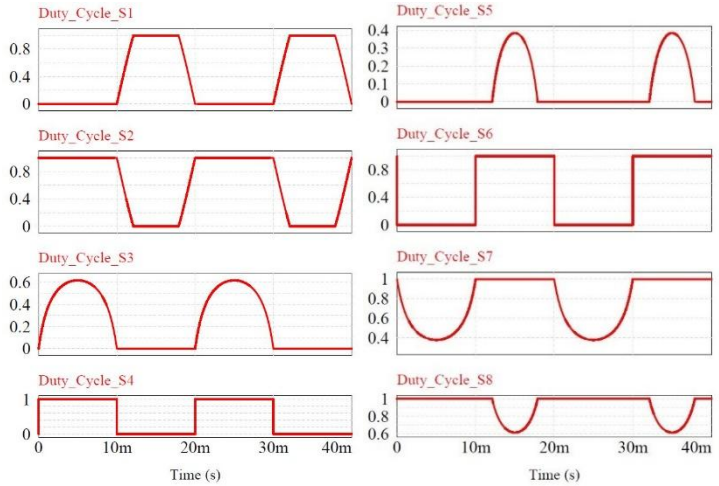

Fig. 5. (a) Duty cycle waveform of switches S_1-S_4, (b) duty cycle waveform of switches S_5-S_8.

mode. In this operating mode, switches S_1, S_7, and S_8 are on and cause the current of inductor L to increase because the input voltage is greater than the instantaneous value of $|V_{out}|$. Fig. 4(b) shows the equivalent circuit of the proposed converter in buck mode and in a freewheeling state. In this operating mode, switches S_2, S_7, and S_8 are on and create a path for the current of inductor L to pass. Although switch S_6 is on during this entire interval, no current passes through it.

F. Asymmetric conditions, negative half cycle, and boost mode

In the negative half-scale and when the instantaneous value of the voltage $|V_{out}|$ is greater than the input voltage, this operation mode occurs. The equivalent circuit of the proposed converter in active state and boost mode is shown in Fig. 4(c). Switches S_1, S_5, and S_6 are on and charge inductor L from the input source. The current of the output passes through capacitor C_f. Although switch S_7 is on, its current is zero. In boost mode, the freewheeling state is shown in Fig. 4(d). Switches S_1, S_7, and S_8 are on and pass the current of inductor L. Switch S_6 is on, but its current is zero. Although Fig. 4(a) and 4(d) are equal, in Fig. 4(a), the inductor current is increasing, and in Fig. 4(d), the inductor current is decreasing. Table I presents the duty cycle of each switch for the positive and negative half-cycles of the output voltage. According to this table, during the positive half-cycle, regardless of the DC input voltage level, the duty cycle for the switches is either $d_{Buck\text{-}Boost}(t)$ or $1\text{-}d_{Buck\text{-}Boost}(t)$, where $d_{Buck\text{-}Boost}(t)$ is defined in (4). The duty cycle in the negative half-cycle varies for the switches and depends on the DC input voltage level. If the absolute value of the instantaneous output voltage is greater than the DC input voltage level, then the duty cycle of the switches will be either $d_{Buck}(t)$ or $1\text{-}d_{Buck}(t)$. If the absolute value of the instantaneous output voltage is less than the DC input voltage level, then the duty cycle will be either $d_{Boost}(t)$ or $1\text{-}d_{Boost}(t)$. The values for $d_{Buck}(t)$ and $d_{Boost}(t)$ are given in (5) and (6), respectively. The duty cycle waveforms of the switches are shown in Fig. 5. These waveforms have been drawn based on the data presented in Table I. Fig. 5(a) shows the duty cycles related to switches S_1–S_4, while Fig. 5(b) shows the duty cycles of switches S_5–S_8. It is worth noting that Table I is very useful for practical implementation and generating PWM pulses in the microcontroller.

IV. Design Guidelines

In this section, the calculation of the duty cycle in different operating modes, the design of inductor L and the output capacitor C_f, as well as the calculation of the voltage stress and the current stress of the switches are discussed.

A. Duty cycle calculation

In unity power factor mode, the voltage and output current equation of the proposed converter in DC-AC operating mode is expressed as:

$$v_{out}(t) = V_{out,\max}\sin(\omega t) \tag{1}$$

$$i_{out}(t) = I_{out,\max}\sin(\omega t) \tag{2}$$

where, $V_{out,max}$ and $I_{out,max}$ are the peak output voltage and current. In order to calculate the switching duty cycle in the buck-boost mode, the volt-second balance law (VSBL) in a full switching period for inductor L is written as:

$$\frac{|v_{out}(t)|}{V_{in}} = \frac{d_{Buck-Boost}(t)}{1-d_{Buck-Boost}(t)} \tag{3}$$

where $d_{Buck\text{-}Boost}$ is duty cycle of the converter in Buck-Boost mode. By simplifying (3), the duty cycle in buck-boost mode can be calculated as:

$$d_{Buck-Boost}(t) = \frac{|v_{out}(t)|}{|v_{out}(t)|+V_{in}} = \frac{V_{out,\max}|\sin(\omega t)|}{V_{out,\max}|\sin(\omega t)|+V_{in}} \tag{4}$$

By applying VSBL to inductor L in buck and boost modes, the switching duty cycle for buck and boost modes can be calculated as:

$$d_{Buck}(t)=\frac{|v_{out}(t)|}{V_{in}}=\frac{V_{out,\max}\left|\sin(\omega t)\right|}{V_{in}} \tag{5}$$

$$d_{Boost}(t)=\frac{|v_{out}(t)|-V_{in}}{|v_{out}(t)|}=\frac{V_{out,\max}\left|\sin(\omega t)\right|-V_{in}}{V_{out,\max}\left|\sin(\omega t)\right|} \tag{6}$$

In equations (5) and (6), d_{Buck} and d_{Boost} are duty cycles of the converter in Buck and Boost modes. The dynamic voltage gain of the proposed converter in the three operating modes, Buck, Boost, and Buck-Boost, is presented in equations (7)–(9).

$$g_{Buck}=\frac{|v_{out}|}{V_{in}}=d_{Buck} \tag{7}$$

$$g_{Boost}=\frac{|v_{out}|}{V_{in}}=\frac{1}{1-d_{Boost}} \tag{8}$$

$$g_{Buck\_Boost}=\frac{|v_{out}|}{V_{in}}=\frac{d_{Buck\_Boost}}{1-d_{Buck\_Boost}} \tag{9}$$

In equations (7) to (9), g_{Buck}, g_{Boost}, and g_{Buck_Boost} are the voltage gain of the converter in Buck, Boost, and Buck-Boost operating modes, respectively. The duration of active mode (t_{on}) and freewheeling mode (t_{off}) in each of the buck, boost, and buck-boost operating modes is calculated as:

$$t_{on,Buck}(t)=\frac{d_{Buck}(t)}{f_S}=\frac{V_{out,\max}\left|\sin(\omega t)\right|}{f_S\cdot V_{in}} \tag{10}$$

$$t_{off,Buck}(t)=\frac{1-d_{Buck}(t)}{f_S}=\frac{V_{in}-V_{out,\max}\left|\sin(\omega t)\right|}{f_S\cdot V_{in}} \tag{11}$$

$$t_{on,Boost}(t)=\frac{d_{Boost}(t)}{f_S}=\frac{V_{out,\max}\left|\sin(\omega t)\right|-V_{in}}{f_S\cdot V_{out,\max}\left|\sin(\omega t)\right|} \tag{12}$$

$$t_{off,Boost}(t)=\frac{1-d_{Boost}(t)}{f_S}=\frac{V_{in}}{f_S\cdot V_{out,\max}\left|\sin(\omega t)\right|} \tag{13}$$

$$t_{on,Buck-Boost}(t)=\frac{d_{Buck-Boost}(t)}{f_S}=\frac{V_{out,\max}\left|\sin(\omega t)\right|}{f_S\left(V_{in}+V_{out,\max}\left|\sin(\omega t)\right|\right)} \tag{14}$$

$$t_{off,Buck-Boost}(t)=\frac{1-d_{Buck-Boost}(t)}{f_S}=\frac{V_{in}}{f_S\left(V_{in}+V_{out,\max}\left|\sin(\omega t)\right|\right)} \tag{15}$$

In the above relationships, $t_{on\text{-}Buck}$, $t_{on\text{-}Boost}$, and $t_{on\text{-}Buck\text{-}Boost}$ represent the active state duration in Buck, Boost, and Buck-Boost operating modes, respectively. Also, $t_{off\text{-}Buck}$, $t_{off\text{-}Boost}$, and $t_{off\text{-}Buck\text{-}Boost}$ represent the freewheeling state duration in Buck, Boost, and Buck-Boost operating modes, respectively, and f_S is the switching frequency.

B. Calculation of flying inductor L

The value of inductor L can be calculated for three operating modes: buck, boost, and buck-boost. Since inductor L has the highest current ripple in buck-boost mode, therefore buck-boost mode is used to calculate the value of this inductor. In the buck-boost mode, the current ripple of inductor L is expressed as:

$$\Delta i_L(t)=\frac{V_{in}\cdot d_{Buck-Boost}(t)}{f_S\cdot L}=\frac{V_{in}\cdot V_{out,\max}\left|\sin(\omega t)\right|}{f_S\cdot L\cdot\left(V_{out,\max}\left|\sin(\omega t)\right|+V_{dc}\right)} \tag{16}$$

At the unity power factor and the instant ωt=π/2, the output instantaneous power has its maximum value, and the current ripple of inductor L is at its maximum value. As a result, L is calculated as:

$$L=\frac{V_{in}\cdot V_{out,\max}}{f_S\cdot\Delta I_{L,\max}\cdot\left(V_{out,\max}+V_{dc}\right)} \tag{17}$$

where, $\Delta I_{L,\max}$ is the maximum current ripple of inductor L. The maximum switching duty cycle in buck-boost mode is expressed as:

$$D_{Buck-Boost,\max}=\frac{V_{out,\max}}{V_{out,\max}+V_{in}} \tag{18}$$

The maximum current ripple of the inductor L based on the output power P_{out} is expressed as:

$$\Delta I_{L,\max}=K_{L,\max}I_{L,\max}=K_{L,\max}\cdot\frac{I_{out,\max}}{1-D_{Buck-Boost,\max}} \tag{19}$$

where $K_{L,max}$ is the ripple percentage of the inductor current. By inserting (18) into (19), the following relation can be obtained.

$$\Delta I_{L,\max}=\frac{2K_{L,\max}\cdot P_{out}\cdot\left(V_{in}+V_{out,\max}\right)}{V_{in}\cdot V_{out,\max}} \tag{20}$$

Finally, by inserting (20) into (17), L is calculated based on the output power and current ripple percentage:

$$L=\frac{\left(V_{in}\cdot V_{out,\max}\right)^2}{2K_{L,\max}\cdot P_{out}\cdot f_S\cdot\left(V_{out,\max}+V_{dc}\right)^2} \tag{21}$$

C. Calculation of output filter capacitor C_f

Capacitor C_f has the highest voltage ripple in buck-boost operating mode. During the active state interval, the current passing through capacitor C_f is equal to the output current, so the capacitor voltage ripple equation can be written as:

$$\begin{aligned}\Delta v_{Cf}&=\frac{1}{C_f}\int_0^{t_{on,Buck-Boost}}I_{out,\max}\sin(\omega t)dt\\&=\frac{I_{out,\max}}{\omega\cdot C_f}\left(1-\cos\left(\omega t_{on,Buck-Boost}\right)\right)\end{aligned} \tag{22}$$

The maximum $t_{on,Buck\text{-}Boost}$ occurs per $D_{Buck\text{-}Boost,max}$. Therefore, by placing (14) in (22), C_f is calculated as:

$$C_f=\frac{2P_{out}}{(2\pi f_g)\cdot\Delta V_{Cf,\max}\cdot V_{out,\max}}\left(1-\cos\left(\frac{(2\pi f_g)\cdot V_{out,\max}}{f_S\cdot\left(V_{in}+V_{out,\max}\right)}\right)\right) \tag{23}$$

were f_g is the frequency of the output voltage or the frequency of the grid and $\Delta V_{Cf,\max}$ is the maximum voltage ripple of the output capacitor.

D. Voltage and current stress of the power electronic switches

In the proposed converter, the switches charge inductor L from the input source during a portion of the cycle and transfer the stored energy in the inductor to the output filter C_f. Therefore, the current stress of all switches is equal to the current of L. In the same output power, the current value of L in the buck-boost mode is higher than in the buck and boost modes, so the current of L is calculated in the buck-boost mode. The current equation of the L is expressed as follows, based on the output current and ripple of the inductor current:

$$i_L(t) = \frac{i_{out}(t)}{1 - d_{Buck-Boost}(t)} + \frac{\Delta i_L(t)}{2} \tag{24}$$

$$\begin{aligned} I_{L,\max} &= \frac{2P_{out}}{V_{out,\max} \cdot \left(1 - \frac{V_{out,\max}}{V_{out,\max} + V_{in}}\right)} + \frac{K_{L,\max} \cdot P_{out} \cdot \left(V_{out,\max} + V_{in}\right)}{V_{in} \cdot V_{out,\max}} \\ &= P_{out}\left(2 + K_{L,\max}\right) \cdot \left(\frac{V_{in} + V_{out,\max}}{V_{in} \cdot V_{out,\max}}\right) \end{aligned} \tag{25}$$

The maximum current of inductor L occurs in the maximum output current, maximum duty cycle, and maximum inductor current ripple. Therefore, the maximum current of inductor L can be calculated in (25). The voltage stress of the switches in the proposed converter is shown in Table II. The voltage stress of switches S_4, S_5, and S_8 is different when the input voltage is lower than the peak of the output voltage and when the input voltage is higher than the peak of the output voltage.

TABLE II.
VOLTAGE STRESS OF SWITCHES USED IN THE PROPOSED CONVERTER.

Switches	$V_{in}<V_{out,max}$	$V_{in}>V_{out,max}$
V_{S1}	V_{in}	V_{in}
V_{S2}	V_{in}	V_{in}
V_{S3}	$V_{in}+V_{out,max}$	$V_{in}+V_{out,max}$
V_{S4}	$V_{out,max}-V_{in}$	0
V_{S5}	$V_{out,max}$	V_{in}
V_{S6}	$V_{out,max}$	$V_{out,max}$
V_{S7}	$V_{in}+V_{out,max}$	$V_{in}+V_{out,max}$
V_{S8}	$V_{out,max}$	0

V. COMPARISON STUDY

In this section, the proposed converter is compared with other converters. In the experimental setup of the converters proposed in other papers, different equipment, and components have been used, and these converters are made in different powers, so it is not possible to make a fair comparison of the reported results in the papers. For the comparison between converters to be completely identical and fair, all converters compared are simulated in the same conditions by PSIM software. In this simulation, the input voltage for all converters is equal to 200V and the output voltage is equal to 230V rms. The output frequency is 32kHz and the output power is 1.5kW. Considering the value of 500µH for inductor L, its current ripple in 1.5kW is about 30.7%. The value of the output filter capacitor is considered equal to 10µF, whose voltage ripple is about 5.8%. Also, the ripple value of the output load current is equal to 5.8%. Considering the same current ripple percentage for inductors and the same voltage ripple percentage for capacitors, the values of inductors and capacitors of other converters are given in Table III.

TABLE III
THE VALUES OF THE PASSIVE COMPONENTS IN THE COMPARED CONVERTERS

Topologies		Values of passive components
JESTPE- [34]	Type-I	L_1=500µH, L_f=370µH, C_f=3.3µF
	Type-II	L_1=500µH, L_f=370µH, C_f=3.3µF
	Type-III	L_1=500µH, L_f=370µH, C_f=3.3µF
	Type-IV	L_1=500µH, L_f=370µH, C_f=3.3µF
TIE- [33]		L_1=521.67µH, L_2=500µH, L_f=370µH, C_2=15µF, C_f=3.3µF
TIE- [32]		L_1=500µH, L_f=370µH, C_f=3.3µF
TIE- [12]		L_1=500µH, L_f=370µH, C_f=3.3µF
TPEL [35]		L_1=500µH, L_2=500µH, L_f=370µH, C_f=3.3µF
TIE- [28]		C_1=22µF, C_2=30µF, C_f=3.3µF, L_f=1.5mH
TEC- [23]		C_1=25µF, C_2=25µF, C_3=60µF, L_f=1.5mH
Modified-Alborg- [30]		C_1=10mF, C_2=10mF, L_1=L_2=210µH, C_f=3.3µF, Lf=370µH
IET- [27]		C_1=25µF, C_2=25µF, C_f=3.3µF, L_f=1.5mH

During the simulation, the internal resistance of the switches and diodes is 50mΩ and the internal voltage drop of the diodes is 0.7V. The internal resistance for low-value capacitors, which can be film capacitors, is about 10mΩ, and for high-value capacitors, which are electrolytic, about 0.1Ω. Also, the internal resistance for the inductor with a value of 500µH is considered to be around 75mΩ, and the internal resistance of other inductors is updated by the following relation:

$$\frac{R_{new}}{R_{old}} = \sqrt{\frac{L_{new}}{L_{old}}} \tag{26}$$

In the above relation, the R_{old} resistance is equal to 75mΩ, and R_{new} is the updated value of the internal resistance of the new inductor. A good way to compare converters in terms of the volume of passive components is to calculate the total maximum energy stored in inductors and capacitors, which is calculated by the following relationships:

$$Vol_L \cong W_L = 0.5 \times \sum_{i=1}^{N_L} L_i \cdot I_{L,\max}^2 \tag{27}$$

$$Vol_C \cong W_C = 0.5 \times \sum_{i=1}^{N_C} C_i \cdot V_{C,\max}^2 \tag{28}$$

In relations (27) and (28), W_L is the total maximum energy stored in the inductors of the converter and W_C is the total maximum energy stored in the capacitors of the converter. N_L and N_C are the number of inductors and capacitors of converters. Also, $I_{L,max}$, and $V_{c,max}$ are the maximum current of inductors and the maximum voltage of capacitors. To calculate total standing voltage (TSV) in converters, (29) is used, which is given below:

$$TSV = \frac{\sum_{i=0}^{N_D+N_S} V_i}{V_{in}} \tag{29}$$

In relation (29), N_S and N_D are the number of switches and diodes of converters. Table IV shows the comparison between the proposed converter and other converters. The parameters compared in this table are the number of switches, the number of diodes, the number of inductors, the number of capacitors, the total maximum energy stored in inductors and capacitors, TSV, boosting factor, conduction losses, efficiency under the same condition, reported efficiency, and also the common coupling capability between input and output.

This article has been accepted for publication in IEEE Transactions on Power Electronics. This is the author's version which has not been fully edited and content may change prior to final publication. Citation information: DOI 10.1109/TPEL.2025.3591384

TABLE. IV
COMPARISON TABLE BETWEEN PROPOSED CONVERTER AND OTHER CONVERTERS.

Topologies		N_S	N_D	N_C	N_L	W_L (mJ)	W_C (J)	TSV (p.u.)	Boosting factor	P_{CON} (W)	Efficiency under the same conditions	Reported Efficiency%	Common Coupling (Input-Output)
JESTPE-[34]	Type-I	9	-	1	2	175	0.1743	14.375	d/(1-d)	67.69	94.92 %	-	Yes
	Type-II	7	-	1	2	172.8	0.1743	12.375	d/(1-d)	56.66	95.43 %	-	No
	Type-III	8	-	1	2	173.8	0.1743	13.375	d/(1-d)	65.74	94.96 %	96% @2.5kW	Yes
	Type-IV	8	-	1	2	158.8	0.1743	12.75	d/(1-d)	61.83	95.21 %	-	Yes
TIE- [33]		6	-	2	3	228.7	0.4743	11.13	d/(1-d)	41.71	96.6 %	95.5% @2.9kW	Yes
TIE-[32]		10	-	1	2	176.4	0.1743	14.375	d/(1-d)	74.8	94.38 %	94.2% @0.3kW	Yes
TIE- [12]		6	-	1	2	171.4	0.1743	11.75	d/(1-d)	47.24	95.96 %	-	No
TPEL[35]		8	4	1	3	336.1	0.1743	15.75	d/(1-d)	74.31	94.81 %	96% @0.5kW	No
TIE- [28]		8	-	3	1	68.5	2.886	17	2d	56.7	95.05 %	97.1% @1.5kW	Yes
TEC- [23]		6	3	4	1	70.2	7.474	18	2d	71.6	92.8 %	97.9% @0.5kW	Yes
Modified-Alborg- [30]		6	4	3	3	221.7	100.17	11.71	d/(1-d)	91.73	91.71 %	98% @0.8kW	No
IET- [27]		6	2	3	1	68.5	2.5	12	2d	59.19	94.95 %	98.1% @0.5kW	Yes
Proposed		8	-	1	1	149.9	0.5281	12.75	d/(1-d)	38.78	96.66 %	97.64%@2.91kW	Yes

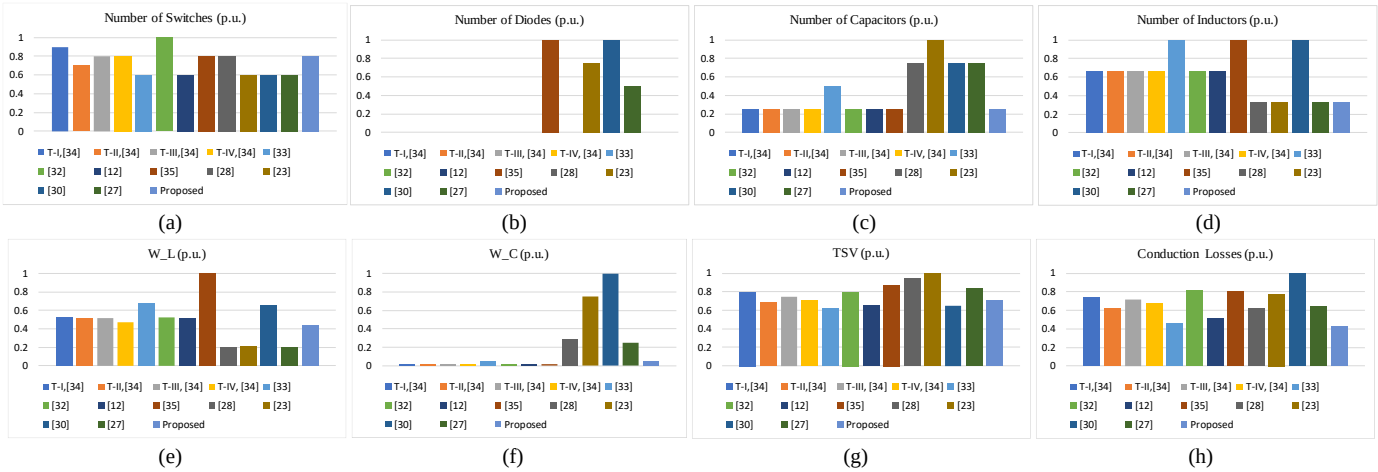

Fig. 6. Comparison between proposed converter and other converters: (a) number of switches, (b) number of diodes, (c) number of capacitors, (d) number of inductors, (e) maximum stored energy in inductors (W_L), (f) maximum stored energy in capacitors, (W_C) (g) total standing voltage (TSV), and (h) conduction losses.

Type-I, Type-III, and Type-IV converters in [34], although in terms of the maximum stored energy in capacitors, they have a lower value than the proposed converter, but each of these converters has one more inductor. Also, in terms of the maximum stored energy in the inductors, they have more value than the proposed converter. The conduction losses of these converters are high compared to the proposed converter, and the TSV of Type-I and Type-III converters is also higher than the proposed converter. The Type-I converter has one more switch than the proposed converter. Although the Type-II converter has one less switch than the proposed converter, and also has less TSV and maximum stored energy in capacitors, but it has one more inductor than the proposed converter, its conduction losses are higher and the common coupling between the input and the output is not established. Although the converter [33] has two switches less than the proposed converter, and in terms of TSV and maximum stored energy in capacitors, it is a little low, but it has two inductors and one more capacitor, it has high conduction losses and in terms of maximum stored energy in the inductors has a higher value than the proposed converter. In terms of the maximum stored energy in capacitors, the converter [32] has a lower value than the proposed converter, but it has two switches and one inductor more than the proposed converter. Also, conduction losses, TSV and the maximum stored energy in the inductors of this converter are more than the proposed converter. The converter [12] has fewer switches than the proposed converter, and the maximum stored energy in capacitors and TSV of this converter is also lower. Instead, it has one more inductor than the proposed converter, it has high conduction losses and the maximum stored energy inside the inductors of this converter is more than the proposed converter. Also, in this converter, a common coupling between input and output is not established. In the converter [35], although the maximum stored energy in capacitors is low compared to the proposed converter, the maximum stored energy in inductors is very high, conduction losses and TSV are high, and it has four diodes and two inductors more than the proposed converter. Converters [23] and [28] are of SC type. Although the maximum stored energy in the inductors of these converters is low compared to the proposed converter, the maximum stored energy inside the capacitors of these converters is very high. TSV and conduction losses are higher, the number of capacitors is higher and their voltage gain is limited. Although the converter [23] has two switches less than the proposed converter, but instead it has three more diodes than the proposed converter. Despite the low number of switches and TSV in the converter [30], the number of diodes, capacitors, and inductors is more than the proposed converter. Also, this converter has higher conduction losses and the maximum stored energy in inductors and capacitors in this converter is more than the proposed converter. Finally, although the converter [27] has two switches less than the proposed converter, the maximum stored energy in inductors and TVS is lower. Instead, it has two diodes and two more capacitors than the proposed converter, the maximum stored energy in the capacitors is high, it has more conduction losses than the proposed

This article has been accepted for publication in IEEE Transactions on Power Electronics. This is the author's version which has not been fully edited and content may change prior to final publication. Citation information: DOI 10.1109/TPEL.2025.3591384

converter, and it also has a limited voltage gain. In order to better understand the comparison table, Fig. 6 is given. It should be noted that this figure was drawn directly from the information in Table IV. According to the efficiency factor under the same condition in Table IV, it is observed that the proposed converter has the highest efficiency compared to other converters. It is noted that this efficiency has been obtained for all converters under the same conditions. If the reported efficiency factor is also considered, it is observed that at around 2.9 kW power, the proposed converter has the highest efficiency. A notable feature that can be stated for the proposed converter in comparison with the converters in [33] and [34] is its flatter efficiency curve. If Figs. 15(a) and 15(b) as well as Fig. 16 of the proposed converter are compared with the efficiency shown in the converters [33] and [34], it is observed that the experimental efficiency in the proposed converter is flatter than these references. In other words, the proposed converter has high efficiency in a wide range of output power, while the converters [33] and [34] only show high efficiency around 1 kW power and have lower efficiency than the proposed converter at other power outputs.

VI. Control System Explanation

A general block diagram of the proposed control strategy for the proposed solution is presented in Fig. 7. In this study, several possible control modes are considered. Before the solid-state circuit breaker (SSCB) connection, the control system determines what type of grid is available. The phase-locked loop (PLL) provides synchronization in the case of an AC grid connection. SSCB is connected to the grid in the case of voltage zero crossing detection and starts working properly with the AC grid-connected algorithm. If the PLL did not detect the AC grid, the control system will check the DC voltage. If the DC grid is detected, the control system recharges the capacitor C_f to the same voltage level, and SSCB switches on with the appropriate DC current control mode. In a very general case, the grid current controller for both the DC and the AC grid can be realized in many ways. It does not need any additional computational resources because only one (DC or AC) strategy is utilized at any moment of time. The control system can inject both DC and AC harmonics, which in turn, is used to detect islanding operation. If the islanding operation is detected, the converter has to stop and relaunch after corresponding external permission in the grid-forming operation. In solar energy applications, the maximum power point tracking (MPPT) block is used for adjusting the reference grid current $i_{g,ref}$ according to the operation point observed on the PV array. This approach is similar to any solar converter. In the battery application, this control block is replaced by the reference current generation considering measured voltage and current (V_{in} and I_{in}). In the AC grid connection, the AC reference grid current $i_{g,ref}$ is elaborated by means of reference peak current $I_{g,max}$ multiplication with a sinusoidal signal from the PLL block. By the scalable factors, the waveform of the reference $i_{g,ref}$ is synchronized with the fundamental component from the voltage at the point of common coupling (PCC) (vg). The reference $i_{g,ref}$ subtracted by the real grid current i_g is given to the current control block. The current controller output (Δv_g) and grid voltage v_g provide the *duty cycle* to be realized across the output capacitor C_f. In order to realize this voltage, the intermediate calculation block is utilized. Taking into account the measured input voltage, using the duty cycle equations, the block defines the value of the corresponding duty cycles. These values are given to the conventional pulse width modulation (PWM) blocks. The MPPT and PLL blocks are not discussed in detail here. A conventional second-order generalized integrator (SOGI) regulator is one the best options for PLL. Similarly, the most common methods for the realization of MPPT are the perturb and observe (P&O) or incremental conductance (IC). Some of the studies utilize modifications of the P&O or IC MPPT methods. There are many options for realizing the grid current control. In this case, the proportional-resonant and repetitive (PRR) controller is utilized for the AC mode, and a simple PI is used for the DC mode. It should be mentioned that alternative nonlinear methods, such as model predictive control (MPC), can be utilized as well.

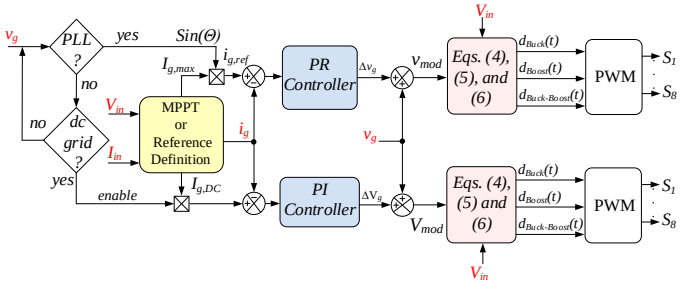

Fig. 7. Control circuit of the proposed universal converter in DC-DC/AC applications.

VII. Experimental Validation

The performance and capabilities of the proposed converter are validated by experimental results in this section. The parameters of active and passive components used in the experimental setup are given in Table V. The experimental setup is shown in Fig. 8. The TMS320F280049 microcontroller was used to generate PWM pulses and control the proposed converter. A programmable DC power supply 62100H-600 from Chroma was used as an input voltage source (PV Simulator). YOKOGAWA-WT1800 power analyzer was used to measure the efficiency of the converter at different operating points. Tektronix-MDO4054-3 oscilloscope was used to capture the experimental waveforms. Tektronix-TCPA300 current probe and Tektronix TPA-BNC voltage probe were used to measure voltages and currents. In this converter, only a 22µF film capacitor is used for the output filter, and the output load is resistive. Fig. 9(a) shows the output voltage (V_{out}), output current (I_{out}), inductor current, and input voltage. In Fig. 9(a), the converter is in symmetric conditions and the inductor current has the same value in the positive and negative half cycles. The proposed converter works like a buck-boost converter in the positive and negative half cycles. The peak value of the output voltage is 325V (230V rms) and the peak value of the output current is 16.6A.

TABLE V
EXPERIMENTAL PARAMETERS

Element	Type
Input voltage (V_{in})	100-400V DC
Output voltage peak value (V_{out})	325V (DC-AC), 350V (DC-DC)
Switching frequency	32kHz
Output power (P_{out})	3kW (DC-AC), 7kW (DC-DC)
Power switches	SanRex (FMG50AQ120N6)
Flying Inductor (L)	334.8 µH
Output filter capacitor (C_f)	22 µF-450V
Gate Driver	ACPL-H342
Isolated DC-DC converter	MGJ2D121505SC

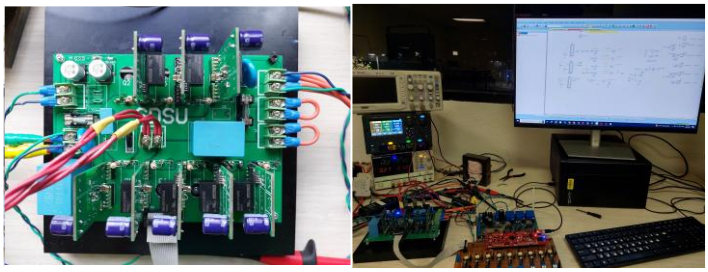

Fig. 8. Laboratory prototype of the proposed converter.

Therefore, the output power is 2.7kW. The input voltage is 400V and the converter is in buck mode. Fig. 9(b) shows the output voltage V_{out}, inductor current, input voltage, and input current. The output power is 2.7kW and the input voltage is 400V. Fig. 9(c) shows the output voltage V_{out}, output current I_{out}, inductor current, and input voltage in asymmetric conditions. The input voltage is 400V and the output power is 2.7kW. Since the converter is in asymmetric conditions, the performance in the positive half-cycle is the same as the buck-boost converter, and in the negative half-cycle, it is the same as the buck converter. Despite the asymmetry of the current of the inductor L in the positive and negative half cycles, the output voltage and current are symmetrical and sinusoidal. Fig. 9(d) shows the output voltage V_{out}, inductor current L, input voltage $V_{in,}$ and input current where the output power is 2.7kW and the input voltage is 400V. According to Fig. 9(b) and 9(d), it can be seen that the input current of the converter is different in symmetric and asymmetric conditions. Since at the same output power, the current of inductor L in asymmetric conditions is lower than that in symmetric conditions, the efficiency of the converter in asymmetric conditions is higher than that in symmetric conditions.

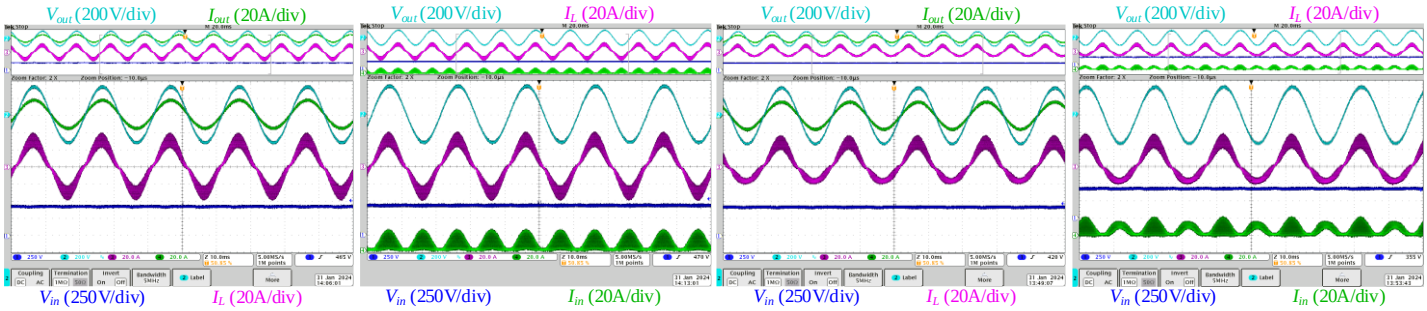

(a) (b) (c) (d)

Fig. 9. V_{in}=400V, V_{out}=230V rms, P_{out}=2.7kW. Symmetric conditions: (a) input voltage, flying inductor current, output voltage, and output current, (b) input voltage, input current, flying inductor current, and output voltage. Asymmetric conditions: (c) input voltage, flying inductor current, output voltage, and output current, (d) input voltage, input current, flying inductor current, and output voltage.

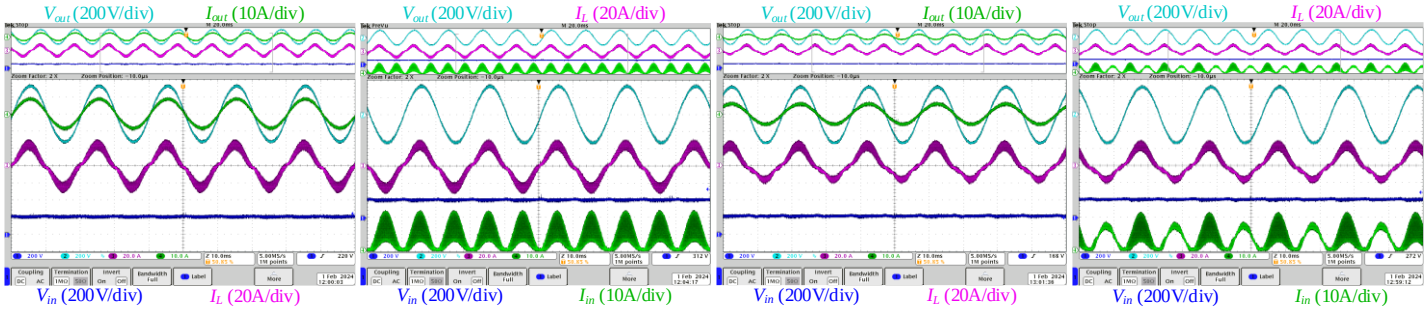

(a) (b) (c) (d)

Fig. 10. V_{in}=200V, V_{out}=230V rms, P_{out}=1.5kW. Symmetric conditions: (a) input voltage, flying inductor current, output voltage, and output current, (b) input voltage, input current, flying inductor current, and output voltage. Asymmetric conditions: (c) input voltage, flying inductor current, output voltage, and output current, (d) input voltage, input current, flying inductor current, and output voltage.

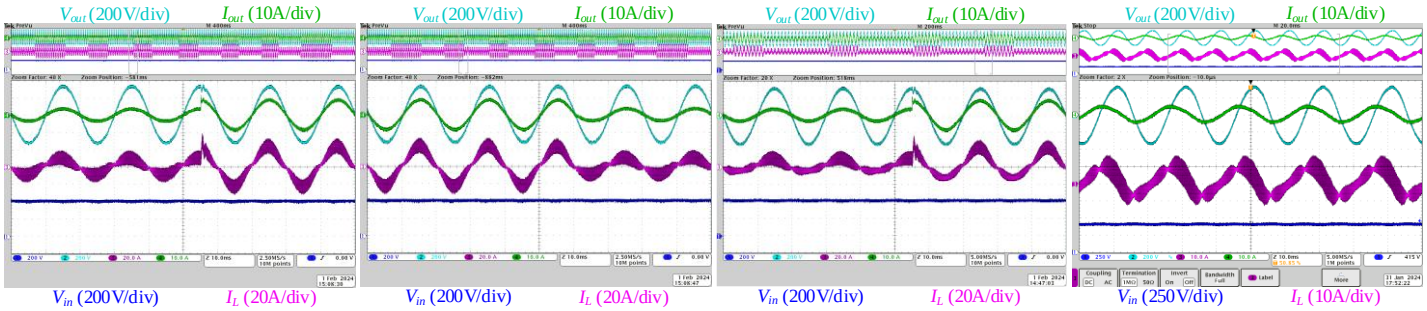

(a) (b) (c) (d)

Fig. 11. Step change conditions: input voltage (400V), flying inductor current, output voltage, and output current, symmetric conditions: (a) output power from 0.8kW to 2kW, (b) output power from 2kW to 0.8kW, (c) asymmetric conditions and output power from 0.8kW to 2kW, (d) non-unity power factor load with the power of 0.83kVA and PF=0.32 lead.

Considering that the converter has the ability to increase the voltage, therefore it can inject power to the output at input voltages lower than the peak output voltage. For this purpose, Fig. 10 is given.

Fig 10(a) shows the output voltage V_{out}, output current I_{out}, inductor current I_L, and input voltage. In this figure, the input voltage is 200V and the peak output voltage is 325V. The output power is 1.5kW.

Fig. 10(b) shows the output voltage, inductor current, input voltage, and input current. The input voltage is 200V and the output power is 1.5kW. In Fig. 10(a) and 10(b), the converter is in symmetric conditions. Considering that the input voltage is lower than the peak output voltage, the converter works in boost mode. In order to show the performance of the converter in boost mode and asymmetric conditions, Figs 10(c) and 10(d) are given. In these figures, the input voltage is 200V and the output power is 1.5kW. The inductor current in the positive half cycle is the same as symmetric conditions, but in the negative half cycle, the conditions are different. In the negative half cycle and as long as the output voltage is less than the input voltage, the converter is in buck mode and when the output voltage is greater than the input voltage, the converter is in boost mode. Fig. 10(c) shows the output voltage and current, inductor current, and input voltage. Fig. 10(d) shows the output voltage, inductor current L, input voltage $V_{in,}$ and input current I_{in}. Since the load connected to the output of the converter can have sudden changes, the proposed converter must be able to keep its output voltage constant during sudden changes in the output load and preserve its stability. To show this capability of the converter, the performance of the converter in step change conditions is given. Fig. 11(a) shows the converter in symmetric condition and the output power was increased from 0.8kW to 2kW. This step change occurred around ωt=90 degrees and shows that the output voltage of the inverter is stable. Fig. 11(b) shows the output power change from 2kW to 0.8kW. It can be seen that overvoltage did not occur. Fig. 11(c) shows the step change in output power in asymmetric conditions. In this figure, the output power was changed from 0.8 to 2 kW, and this happened around ωt=90 degrees. It is observed that the output voltage of the inverter is stable.

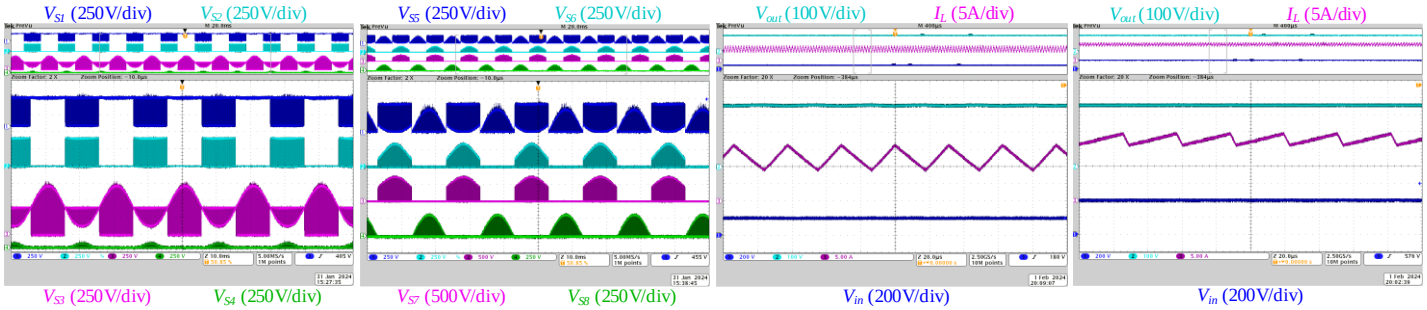

Fig. 12. Voltage stress of switches: (a) V_{S1}-V_{S4}, (b) V_{S5}-V_{S8}. DC-DC operation modes: (c) input voltage, the inductor current and output voltage with V_{in}=200, V_{out}=350V, and P_{out}= 3.13kW, (d) input voltage, the inductor current and output voltage with V_{in}=400, V_{out}=350V, and P_{out}= 6.6 kW.

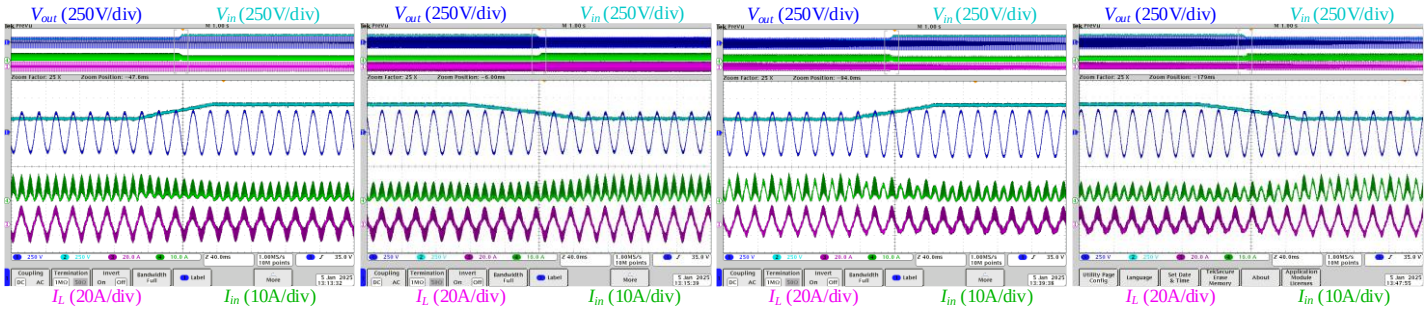

Fig. 13. The input voltage, output voltage, input current, and flying inductor current under the transient conditions of input voltage and with output power of 1.5 kW and output voltage of 230VRMS: (a) input voltage changes from 200V to 400V and in symmetric operation modes (b) input voltage changes from 400V to 200V and in symmetric operation modes, (c) input voltage changes from 200V to 400V and in asymmetric operation modes, and (d) input voltage changes from 400V to 200V and in asymmetric voltage changes.

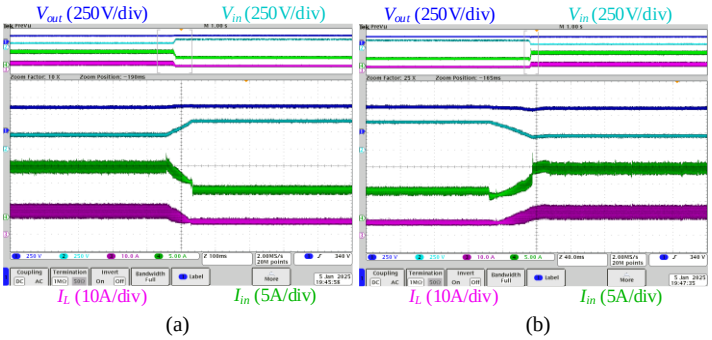

Fig. 14. The output voltage, input voltage, input current, and flying inductor current under the transient conditions of input voltage, DC-DC operation mode and with output power of 3 kW and output voltage of 350VDC: (a) input voltage changes from 200V to 400V, and (b) input voltage changes from 400V to 200V.

Fig. 11(a)-(c) shows the output voltage and current, inductor current, and input voltage. The input voltage value is 400V. Fig. 11(d) shows the capability of the proposed converter under non-unity power factor loads. To create a phase difference between the output voltage and current, a capacitor and an inductor were connected in series with the load resistance. In this figure, the active power is 0.27kW, the reactive power is 0.78kVAR and the apparent power is 0.83kVA. The output power factor is 0.32 lead. From Fig. 11(d), it can be concluded that the proposed converter is able to supply the output load with a very low power factor. Fig. 12(a) and 12(b) show the voltage stress of switches S_1 to S_8. The very appropriate design of the PCB for the power board has made the blocked voltage of the switches without spikes, which is very effective in reducing switching losses. Finally, in order to show the performance of the converter in DC-DC mode and for dual-purpose applications, Fig. 12(c) and 12(d) are given. In Fig. 12(c), the converter is in boost mode. The input voltage is 200V, and the output voltage is 350V. The output power in boost mode is 3.13 kW.

In Fig. 12(d), the converter is in buck mode. The input voltage is 400V, and the output voltage is 350V. The output power is 6.6 kW. To demonstrate the converter's performance in transient conditions, Figs. 13 and 14 are provided. The purpose of these experimental results is to vary the input voltage while maintaining a stable output voltage. A closed-loop control system is used to ensure a constant output voltage under local-load conditions, regardless of input voltage variations. In Fig. 13, the converter operates in DC-AC mode, while in Fig. 14, it operates in DC-DC mode. Since the DC-AC mode includes both symmetric and asymmetric operating conditions, all these cases are illustrated in Fig. 13. Fig. 13(a) shows the input voltage, output voltage, input current, and flying inductor current.

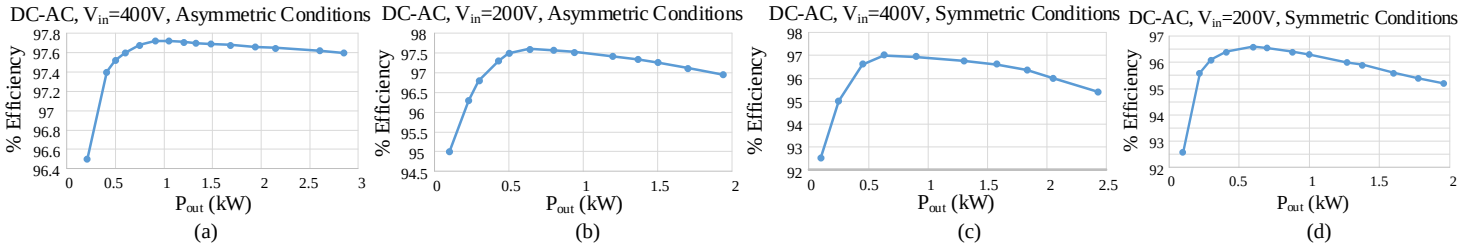

Fig.15. Experimental efficiency in DC-AC modes: (a) asymmetric conditions with V_{in}=400V, (b) asymmetric conditions with V_{in}=200V, (c) symmetric conditions with V_{in}=400V, and (d) symmetric conditions with V_{in}=200V.

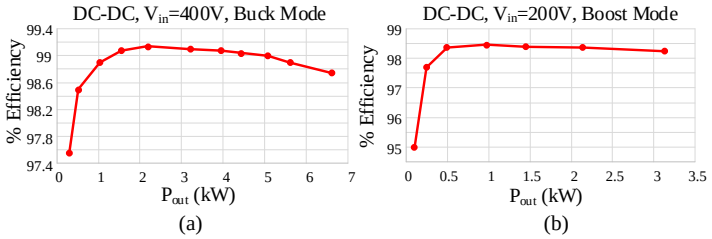

Fig. 16. Experimental efficiency, DC-DC modes: (a) buck mode with V_{in}=400V, (b) boost mode with V_{in}=200V.

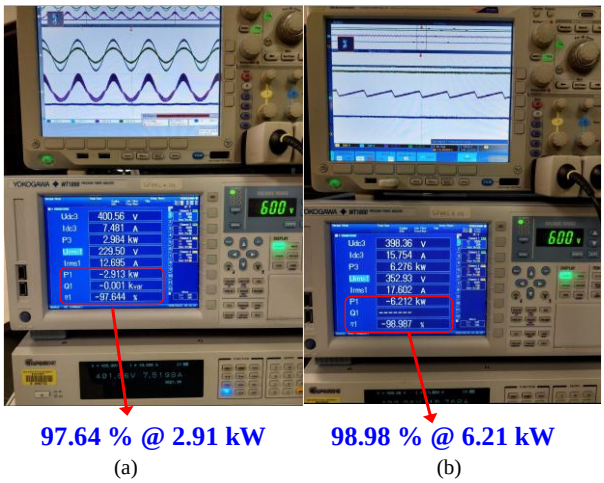

Fig. 17. Power analyzer and oscilloscope screen: (a) DC-AC operation, P_{out}=2.91kW, η=97.64 %, (b) DC-DC operation, P_{out}=6.21kW, η=98.98%.

The input voltage increases from 200V to 400V, while the output voltage (or load voltage) remains constant at its nominal value of 230V RMS. The output power is approximately 1.5 kW. Since the output voltage and power remain unchanged during the input voltage variation process, increasing the input voltage results in a decrease in both the input current and the flying inductor current. In Fig. 13(a), the converter operates in the symmetric mode. Similarly, in Fig. 13(b), the converter remains in symmetric mode. Here, the input voltage decreases from 400V to 200V, while the output voltage remains constant at its nominal value. The output power is also around 1.5 kW. Given that the output voltage and power remain fixed, reducing the input voltage leads to an increase in both the input current and the flying inductor current. In Figs. 13(c) and 13(d), the converter operates in asymmetric mode. These figures also present the input voltage, output voltage, input current, and flying inductor current. The input voltage varies between 200V and 400V, while the output voltage remains at 230V RMS. Additionally, the output power is approximately 1.5 kW. Since the output voltage and power remain constant, increasing the input voltage results in a decrease in the input current and the flying inductor current, whereas decreasing the input voltage causes an increase in both currents. In Fig. 13(c), the input voltage rises from 200V to 400V, while in Fig. 13(d), the input voltage decreases from 400V to 200V. In Fig. 14, the converter operates in DC-DC mode. This figure illustrates the input voltage, output voltage, input current, and flying inductor current. The input voltage varies between 200V and 400V, while the output voltage is maintained constant at 350V DC. The output power is approximately 3 kW. In Fig.14(a), the input voltage increases from 200V to 400V, while the output voltage remains fixed at 350V. Since the output voltage and power remain constant, the input current and flying inductor current decrease. In Fig. 14(b), the input voltage decreases from 400V to 200V, while the output voltage remains at its nominal value. With the output voltage and power remaining constant, the decrease in input voltage leads to an increase in both the input current and the flying inductor current. Figs. 15 and 16 show the efficiency of the converter at different operating conditions. Fig. 15 shows the efficiency of the converter in DC-AC operating conditions and Fig. 16 shows the efficiency of the converter in DC-DC operating conditions. In Fig. 15(a), the experimental efficiency is shown in asymmetric conditions at an input voltage of 400V. The maximum efficiency is 97.7% happened around 1.2kW. In Fig. 15(b), the efficiency is shown in asymmetric conditions at 200V input voltage. The maximum efficiency is 97.6% occurs at the output power of 0.64 kW. Fig. 15(c) shows the efficiency in symmetric conditions at an input voltage of 400V. The maximum efficiency is 97% and occurs at an output power of 0.63 kW. In Fig. 15(d), the experimental efficiency is shown in symmetric conditions at the input voltage of 200. The maximum efficiency is 96.6%, which occurred at an output power of 0.6 kW. Finally, Fig. 16 shows the experimental efficiency in the DC-DC operating mode. Fig. 16(a) is the efficiency diagram in buck mode, and the input voltage is 400V. The maximum efficiency reached 99.14%, which occurred at the output power of 2.16 kW. In Fig. 16(b), the converter is in boost mode, and the input voltage is 200V. An efficiency of 98.46% was achieved at the output power of 1 kW. Fig. 17 shows the efficiency of the converter along with the input

and output powers as well as the waveforms of the oscilloscope. Fig. 17(a) shows the DC-AC mode, and Fig. 17(b) shows the DC-DC mode. To calculate the total volume of the converter, the volume of the inductor, the volume of the capacitors, and the volume of the heatsink have been considered.

$$Volume\_Inductor = L \times W \times H = 11 \times 3.6 \times 11 = 435.6\ cm^3 \quad (30)$$

$$Volume\_Heatsink = 20 \times 20 \times 2.5 = 1000\ cm^3 \quad (31)$$

$$Volume\_Capacitors = 2 \times (2.16 \times 3.1 \times 3.6) = 48.21\ cm^3 \quad (32)$$

$$Total\_Volume = 435.6 + 1000 + 48.21 = 1483.81\ cm^3 \quad (33)$$

Finally, the power density of the prototype is calculated as follows:

$$Power\ density = \frac{P_{out}}{Total\_Volume} = \frac{7000}{1483.81} = 4.72\ W/cm^3 \quad (34)$$

VIII. Conclusion

In this paper, a novel flying-inductor-based single-phase converter topology was proposed. This topology can be used as an interface between AC and DC microgrids. Due to the existence of common coupling between the input and output terminals, the converter can be a suitable solution for RES, especially PV systems. The buck-boost capability of the proposed converter makes it possible to use it at different input voltages while keeping the output voltage constant. The proposed converter topology is a single-stage power processing circuit, which makes it possible to achieve an extremely high efficiency. This feature is evident from the experimental efficiency shown in the experimental section. The experimental results show that the proposed converter is able to feed non-unity power factor loads. Power transfer from the input terminal to the output without the presence of an electrolytic capacitor increases the life of the converter. The operating modes and design of passive elements were discussed in detail. Also, in order to show the advantages of the proposed converter, a comparison was made with other converters. Finally, an experimental setup (3kW/7kW) was carried out and the experimental results validated the proposed converter topology.

Acknowledgment

The authors would like to acknowledge the financial support of the California Energy Commission under grant number EPC-19-053. The authors also appreciate the use of power MOSFETs provided by SanRex in the experimental setup of this work.

References

[1] C.L. Sulzberger, "Triumph of AC. 2. The battle of the currents," *IEEE Power and Energy Magazine*, vol. 1, no. 4, pp. 70-73, 2003.

[2] R. W. De Doncker, "Power electronic technologies for flexible DC distribution grids." *in proc. of IPEC-Hiroshima 2014 - ECCE ASIA*, pp. 736-743.

[3] T. H. Shahsavar et al., "A New Flying Capacitor-Based Buck–Boost Converter for Dual-Purpose Applications," in *IEEE Journal of Emerging and Selected Topics in Industrial Electronics*, vol. 4, no. 2, pp. 447-459, April 2023.

[4] J.D. Paez, D. Frey, J. Maneiro et al., "Overview of DC–DC converters dedicated to HVDC grids," *IEEE Trans. on Power Delivery*, vol. 34, no. 1, pp. 119-128, 2018.

[5] I. Alhurayyis, A. Elkhateb, D.J. Morrow, "Isolated and non-isolated DC-to-DC converters for medium voltage DC networks: A review," *IEEE Journal of Emerg. Sel. Top. Pow. Electron.*, vol. 9, no. 6, pp. 7486-7500, 2021.

[6] S. Beheshtaein, R. M. Cuzner, M. Forouzesh, M. Savaghebi, J.M. Guerrero, "DC microgrid protection: A comprehensive review," *IEEE Journal of Emerg. Sel. Top. Pow. Electron.*, 2019, Early Access.

[7] S. Lu, K. Sun, H. Shi, Y. Li, G. Cao, "Evaluation of high step-up power conversion systems for large-capacity photovoltaic generation integrated into medium voltage DC grids," *Chinese Journal of Electrical Engineering*, vol. 7, no. 4, pp. 3-14, 2021.

[8] S. Cui, N. Soltau, and R. W. De Doncker, "A high step-up ratio soft-switching DC–DC converter for interconnection of MVDC and HVDC grids," *IEEE Trans. on Power Electron.*, vol. 33, no. 4, pp. 2986-3001, 2017.

[9] A. Sannino, G. Postiglione, M. H. J. Bollen, "Feasibility of a DC network for commercial facilities," *IEEE Trans. on Ind. Appl.*, vol. 39, no. 5, pp. 1499–1507, 2003.

[10] D. Boroyevich, I. Cvetkovic, D. Dong, R. Burgos, F. Wang, F. Lee, "Future electronic power distribution systems a contemplative view," *in Proc. of OPTIM*, 2010, pp. 1369–1380.

[11] O. Husev, O. Matiushkin, D. Vinnikov, C. Roncero-Clemente, S. Kouro, "Novel Concept of Solar Converter with Universal Applicability for DC and AC Microgrids," *IEEE Tran. on Ind. Electron.*, vol. 69, no. 5, pp. 4329 - 4341, 2022.

[12] O. Matiushkin, O. Husev, J. Rodriguez, H. Young and I. Roasto, "Feasibility Study of Model Predictive Control for Grid-Connected Twisted Buck–Boost Inverter," in *IEEE Transactions on Industrial Electronics*, vol. 69, no. 3, pp. 2488-2499, March 2022.

[13] F. Z. Peng, "Z-source inverter," *IEEE Trans. on Industry Applications*, vol. 39, no. 2, pp. 504-510, 2003.

[14] A. Chub, D. Vinnikov, F. Blaabjerg, F.Z. Peng "A Review of Galvanically Isolated Impedance-Source DC–DC Converters" *IEEE Trans. Power Electron.*, Vol. 31, N. 4, pp. 2808-2828, April 2016.

[15] O. Husev, D. Vinnikov, C. Roncero-Clemente, A. Chub, E. Romero-Cadaval, "Single-Phase String Solar qZS-based Inverter: Example of Multi-Objective Optimization Design." *IEEE Trans. on Ind. Appl.*, vol. 57, no. 3, pp. 3120 - 3130, May-June. 2021.

[16] D. Panfilov, O. Husev, F. Blaabjerg, J. Zakis, K. Khandakji, "Comparison of three-phase three-level voltage source inverter with intermediate dc-dc boost converter and quasi-Z-source inverter", *IET Power Electron.*, vol. 9, no. 6, pp. 1238-1248, 2016.

[17] X. Guo, "A novel CH5 inverter for single-phase transformerless photovoltaic system applications," *IEEE Trans. Circuits Sys. II: Express Briefs*, vol. 64, no. 10, pp. 1197-1201, Oct. 2017.

[18] X. Guo, "Three-phase CH7 inverter with a new space vector modulation to reduce leakage current for transformerless photovoltaic systems," *IEEE J. Emerg. Sel. Topics Power Electron.*, vol. 5, no. 2, pp. 708-712, Jun. 2017.

[19] J. F. Ardashir, M. Sabahi, S. H. Hosseini, F. Blaabjerg, E. Babaei and G. B. Gharehpetian, "A Single-Phase Transformerless Inverter with Charge Pump Circuit Concept for Grid-Tied PV Applications," *IEEE Trans. Ind. Electron.*, vol. 64, no. 7, pp. 5403-5415, Jul. 2017.

[20] Y. P. Siwakoti and F. Blaabjerg, "Common-ground-type transformerless inverters for single-phase solar photovoltaic systems," *IEEE Trans. Ind. Electron.*, vol. 65, no. 3, pp. 2100-2111, Mar. 2018.

[21] N. Vosoughi, S. H. Hosseini and M. Sabahi, "A New Transformer-Less Five-Level Grid-Tied Inverter for Photovoltaic Applications," *IEEE Trans. Energy Conversion*, vol. 35, no. 1, pp. 106-118, Mar. 2020.

[22] B. Shaffer, H. A. Hassan, M. J. Scott, S. U. Hasan, G. E. Town and Y. Siwakoti, "A Common-Ground Single-Phase Five-Level Transformerless Boost Inverter for Photovoltaic Applications," *in Proc. IEEE Applied Power Electronics Conference and Exposition (APEC), San Antonio, TX*, Mar. 2018, pp. 368-374.

[23] N. V. Kurdkandi et al., "A New Transformer-Less Common Grounded Three-Level Grid-Tied Inverter With Voltage Boosting Capability," *in IEEE Transactions on Energy Conversion*, vol. 36, no. 3, pp. 1896-1909, Sept. 2021.

[24] F. B. Grigoletto, "Five-level transformerless inverter for single-phase solar photovoltaic applications" *IEEE Emerg. and Select. Topics Power Electron.*, vol. 8, no. 4, pp. 3411-3422, Dec. 2020.

[25] N. Sandeep, M. J. Sathik, U. R. Yaragatti, V. Krishnasamy, A. K. Verma and H. R. Pota, "Common-Ground Type Five-Level Transformerless Inverter Topology with Full DC-Bus Utilization," *IEEE Trans. Ind. Applicat*, vol. 56, no. 4, pp. 4071-4080, Jul.-Aug. 2020.

[26] M. Chen, P. C. Loh, Y. Yang, and F. Blaabjerg, "A Six-Switch Seven-Level Triple-Boost Inverter," *IEEE Trans. Power Electron.*, vol. 36, no. 2, pp. 1225-1230, Feb. 2021.

[27] N. Vosoughi, S. H. Hosseini, and M. Sabahi, "Single-phase common-grounded transformer-less grid-tied inverter for pv application," *IET Power Electron.*, vol. 13, no. 1, pp. 157-167, Jan., 2020.

[28] N. Vosoughi, S. H. Hosseini, and M. Sabahi, "A new single-phase transformerless grid-connected inverter with boosting ability and common ground feature," *IEEE Trans. Ind. Electron.*, vol. 67, no. 11, pp. 9313–9325, Nov. 2019.

[29] Zeng, W. Lin and J. Liu, "Switched-Capacitor-Based Active Neutral-Point-Clamped Seven-Level Inverter With Natural Balance and Boost Ability," *IEEE Access*, vol. 7, pp. 126889- 26896, Jul. 2019.
[30] H. Wang, W. Wu, S. Zhang, Y. He, H. S. -H. Chung and F. Blaabjerg, "A modified Aalborg inverter extracting maximum power from one PV array source," in *CPSS Transactions on Power Electronics and Applications*, vol. 4, no. 2, pp. 109-118, June 2019.
[31] J. Falck, C. Felgemacher, A. Rojko, M. Liserre, and P. Zacharias, "Reliability of power electronic systems: An industry perspective," *IEEE Trans Ind. Electron.* Mag., vol. 12, no. 2, pp. 24–35, Jun. 2018.
[32] M. Tofigh Azary, M. Sabahi, E. Babaei, and F. Abbasi Aghdam Meinagh, "Modified single-phase single-stage grid-tied flying inductor inverter with MPPT and suppressed leakage current," *IEEE Trans. Ind. Electron.*, vol. 65, no. 1, pp. 221–231, Jan. 2018.
[33] O. Husev, N. V. Kurdkandi, M. G. Marangalu, D. Vinnikov and S. H. Hosseini, "A New Single-Phase Flying Inductor-Based Common Grounded Converter for Dual-Purpose Application," in *IEEE Transactions on Industrial Electronics*, vol. 70, no. 8, pp. 7913-7923, Aug. 2023.
[34] N. V. Kurdkandi, O. Husev, O. Matiushkin, D. Vinnikov, Y. P. Siwakoti and S. S. Lee, "Novel Family of Flying Inductor-Based Single-Stage Buck–Boost Inverters," *in IEEE Journal of Emerging and Selected Topics in Power Electronics*, vol. 10, no. 5, pp. 6020-6032, Oct. 2022.
[35] H. Wang, W. Wu, J. Zhu, E. Koutroulis, H. S. -H. Chung and F. Blaabjerg, "A Novel Dual Buck and Boost Transformer-Less Single-Phase Grid-Tied Inverter," *in IEEE Trans. Power Electron.*, vol. 37, no. 4, pp. 4211-4224, April 2022.

Naser Vosoughi Kurdkandi (Member, IEEE) received his Ph.D. degree in Electrical Engineering and Power Electronics from the University of Tabriz, Tabriz, Iran, in 2019. From 2019 to 2020, he was a Postdoctoral Researcher at the University of Tabriz. In 2020, he joined Tallinn University of Technology (TalTech), Tallinn, Estonia, as a Postdoctoral Researcher. Since 2022, he has been a Postdoctoral Research Fellow at San Diego State University, San Diego, CA, USA. His research interests include multilevel inverters, grid-connected PV inverters, DC-DC switched-capacitor and switched-inductor converters, fast charging stations for electric vehicles, battery-based energy storage systems, and induction motor drives. Since 2021, he has been recognized as one of the world's top 2% most-cited scientists, according to a global citation-based ranking by Stanford University.

Sze Sing Lee (SM'18) received the B.Eng. (Hons.) and Ph.D. degrees in Electrical Engineering from Universiti Sains Malaysia, Malaysia, in 2010 and 2013, respectively. From 2014 to 2019, he was a Lecturer / Assistant Professor at the University of Southampton Malaysia Campus. From 2018 to 2019, he was a Visiting Research Professor at Ajou University, South Korea. He is currently an Assistant Professor and Degree Program Director of Electrical Power Engineering at Newcastle University in Singapore. His research interests include power converter / inverter topologies and their control strategies. Dr. Lee is an Associate Editor of the IEEE Transactions on Power Electronics and the IEEE Transactions on Industrial Electronics. He is a Chartered Engineer registered with the Engineering Council, UK, and currently serves as a Professional Review Interviewer and International Professional Registration Advisor.

Oleksandr Husev (Senior Member, IEEE) received the Ph.D. degree in industrial electronics from the Institute of Electrodynamics, National Academy of Science of Ukraine, Kyiv, Ukraine, in 2012. Currently, he is a Research Group Leader with the Department of Power Electronics and Electrical Machines, Gdansk University of Technology, Gdansk, Poland. His research interests include applied power electronics systems, modeling, simulation, industrial PCB design and control system implementation, and stability investigation. Dr. Husev has authored and co-authored more than 200 scientific publications and holds several international patents. He was recognized as Best Researcher in his institutions and received Estonian National Award.

Zhi Cao (Member IEEE) received the B.S. and Ph.D. degrees in electrical engineering from Southeast University, Nanjing, China, in 2016 and 2022, respectively. He has been a Postdoctoral Researcher with the Department of Electrical and Computer Engineering, San Diego State University, San Diego, USA, since October, 2022. His main research interests include battery energy storage system, electrical motors and drives, and magnetic bearing system.

Chunting Chris Mi (S'00–A'01–M'01–SM'03–F'12) received the B.S.E.E. and M.S.E.E. degrees in electrical engineering from Northwestern Polytechnical University, Xi'an, China, and the Ph.D. degree in electrical engineering from the University of Toronto, Toronto, Ontario, Canada, in 1985, 1988, and 2001, respectively. He is a fellow of both IEEE and SAE. He is a Distinguished Professor of the Department of Electrical and Computer Engineering and the Director of and Director of Caili & Daniel Chang Center of Electrical Drive Transportation, San Diego State University, San Diego, USA. Prior to joining SDSU, he was with the University of Michigan, Dearborn, from 2001 to 2015. His research interests include electric drives, power electronics, electric machines, electrical and hybrid vehicles, wireless power transfer, and power electronics. He is the recipient of the IEEE PELS Emerging Technology Award in 2019, IEEE Transaction on Power Electronics Best Paper Award, and two IEEE Transaction on Power Electronics Prize Letter Awards. He is the recipient of the Albert W. Johnson Lecture Award which is the highest distinction for any SDSU faculty. In 2023, he received the IEEE PELS Achievement Award in Vehicle and Transportation Systems and the Best Paper Award from IEEE Transactions on Industry Applications.